

ARTICLE

Received 4 Dec 2014 | Accepted 15 Jun 2015 | Published 23 Jul 2015

DOI: 10.1038/ncomms8817

OPEN

Controllable synthesis of molybdenum tungsten disulfide alloy for vertically composition-controlled multilayer

Jeong-Gyu Song¹, Gyeong Hee Ryu², Su Jeong Lee³, Sangwan Sim¹, Chang Wan Lee¹, Taejin Choi¹, Hanearl Jung¹, Youngjun Kim¹, Zonghoon Lee², Jae-Min Myoung³, Christian Dussarrat⁴, Clement Lansalot-Matras⁵, Jusang Park¹, Hyunyong Choi¹ & Hyungjun Kim¹

The effective synthesis of two-dimensional transition metal dichalcogenides alloy is essential for successful application in electronic and optical devices based on a tunable band gap. Here we show a synthesis process for $\text{Mo}_{1-x}\text{W}_x\text{S}_2$ alloy using sulfurization of super-cycle atomic layer deposition $\text{Mo}_{1-x}\text{W}_x\text{O}_y$. Various spectroscopic and microscopic results indicate that the synthesized $\text{Mo}_{1-x}\text{W}_x\text{S}_2$ alloys have complete mixing of Mo and W atoms and tunable band gap by systematically controlled composition and layer number. Based on this, we synthesize a vertically composition-controlled (VCC) $\text{Mo}_{1-x}\text{W}_x\text{S}_2$ multilayer using five continuous super-cycles with different cycle ratios for each super-cycle. Angle-resolved X-ray photo-emission spectroscopy, Raman and ultraviolet-visible spectrophotometer results reveal that a VCC $\text{Mo}_{1-x}\text{W}_x\text{S}_2$ multilayer has different vertical composition and broadband light absorption with strong interlayer coupling within a VCC $\text{Mo}_{1-x}\text{W}_x\text{S}_2$ multilayer. Further, we demonstrate that a VCC $\text{Mo}_{1-x}\text{W}_x\text{S}_2$ multilayer photodetector generates three to four times greater photocurrent than MoS_2 - and WS_2 -based devices, owing to the broadband light absorption.

¹School of Electrical and Electronic Engineering, Yonsei University, Seoul 120-749, Korea. ²School of Materials Science and Engineering, Ulsan National Institute of Science and Technology (UNIST), Ulsan 689-798, Korea. ³Department of Materials Science and Engineering, Yonsei University, Seoul 120-749, Korea. ⁴Air Liquide Laboratories, Wadai 28, Tsukuba, Ibaraki 300-4247, Japan. ⁵Air Liquide Laboratories Korea, Yonsei Engineering Research Park, 50 Yonsei-ro, Seodaemun-gu, Seoul 120-749, Korea. Correspondence and requests for materials should be addressed to H.K. (email: hyungjun@yonsei.ac.kr).

The band gap modulation of two-dimensional (2D) transition metal dichalcogenides (TMDCs) has been intensively studied, because of their various applications in optoelectronic devices such as photodiodes, phototransistors and solar cells^{1–3}. It is well known that the band gap of 2D TMDCs is dependent on the number of layers^{4–6}. In addition, alloying 2D TMDCs through the synthesis of $\text{Mo}_{1-x}\text{W}_x\text{S}_2$, $\text{Mo}_{1-x}\text{W}_x\text{Se}_2$ or $\text{MoS}_{2x}\text{Se}_{2(1-x)}$, for example, is another way of practically modulating the band gap. This is an effective approach because of the good thermodynamic stability at room temperature of the alloys, as predicted by theoretical calculations^{7–14}. Furthermore, recent studies have shown that a vertically composition-controlled (VCC) 2D TMDCs multilayer is feasible for the high performance optoelectronic devices due to functionality of interlayer such as interlayer transition^{15–22}. However, the reported synthesis processes for 2D TMDCs alloy and VCC 2D TMDCs multilayer, such as exfoliation, chemical vapor deposition and transfer, are limited in respect of systematic control of the composition and the number of layers, and clean interface for strong interlayer coupling^{9,11,21,23}. Hence, an improved synthesis process for 2D TMDCs alloy and VCC 2D TMDCs multilayer is highly required.

Atomic layer deposition (ALD), which is based on surface reactions between precursors and reactants, has benefits such as high purity, thickness control on the atomic scale and large area uniformity^{24,25}. In particular, it is suitable for the synthesis of alloy thin films with precisely controlled composition using the super-cycle method^{26–28}. In addition, a continuous super-cycle process with different cycle ratios can produce a VCC multilayer with a clean interface²⁹. In a previous report, we have shown that atomically thin, layer-controlled and wafer-level uniform 2D WS_2 can be synthesized by sulfurization of ALD WO_3 thin films³⁰.

Here we report a synthesis method of $\text{Mo}_{1-x}\text{W}_x\text{S}_2$ alloys by sulfurization of super-cycle ALD $\text{Mo}_{1-x}\text{W}_x\text{O}_y$ alloy thin films. Using this method, we systematically control the composition and layer number (from mono- to tri-layers) of $\text{Mo}_{1-x}\text{W}_x\text{S}_2$ alloys by controlling the cycle ratio between the ALD MoO_x and WO_3 . The bandgaps of the $\text{Mo}_{1-x}\text{W}_x\text{S}_2$ alloys are precisely controlled as functions of the composition and layer numbers of each respective alloy, as measured based on the photoluminescence (PL) spectra. Scanning transmission electron microscopy (STEM) shows the mixing of Mo and W atoms with shared metal atom sites in monolayer $\text{Mo}_{1-x}\text{W}_x\text{S}_2$ alloy. Furthermore, we develop a process to synthesize a VCC $\text{Mo}_{1-x}\text{W}_x\text{S}_2$ multilayer using a sequential super-cycle ALD process—specifically, 5 continuous super-cycles of ALD with different cycle ratios for each super-cycle. Ultraviolet-visible spectrophotometer analysis shows that the synthesized VCC $\text{Mo}_{1-x}\text{W}_x\text{S}_2$ multilayer has stronger interlayer coupling than that of a stacked VCC $\text{Mo}_{1-x}\text{W}_x\text{S}_2$ multilayer fabricated by the individual transfer of each monolayer $\text{Mo}_{1-x}\text{W}_x\text{S}_2$ alloy. This can be attributed to the clean interface between each layer in the synthesized sample^{15,21}.

Results

MoS₂ synthesis. Previously, we reported the synthesis of WS_2 using sulfurization of ALD WO_3 thin film with a one-step sulfurization process at 1,000 °C (ref. 30). These synthesized WS_2 exhibit smooth and continuous surfaces with layer controllability from mono- to tetra-layer. Based on this result, we sulfurized ALD MoO_x thin film (nine cycles, optimization of ALD MoO_x is represented in Supplementary Fig. 1) using a one-step sulfurization process at 1,000 °C (see experimental section) to synthesize MoS_2 . Figure 1a,b comprises scanning electron microscope (SEM) and atomic force microscopy (AFM) images of sulfurized MoO_x thin film using the one-step sulfurization

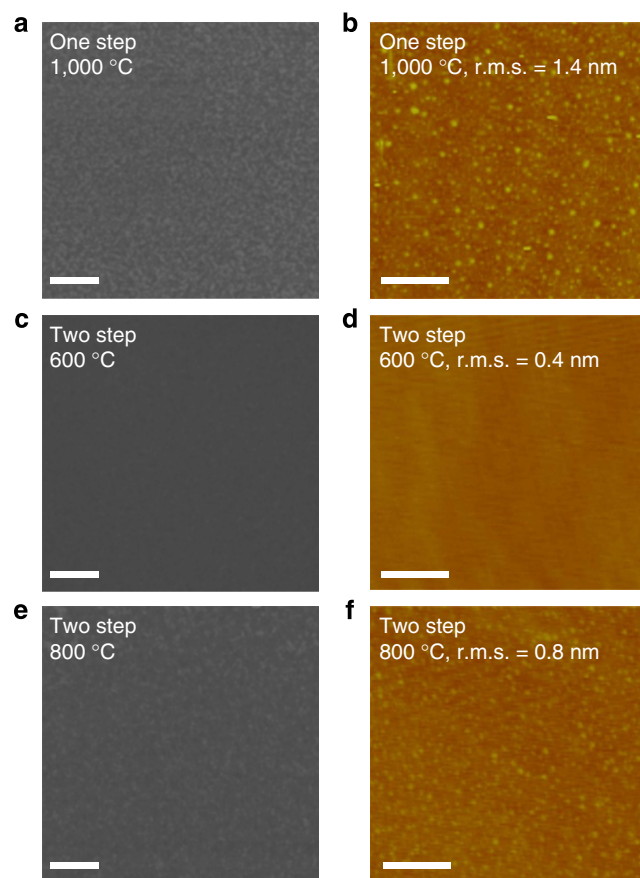


Figure 1 | Sulfurization of MoO_x thin films. (a) SEM and (b) AFM images of sulfurized MoO_x thin film using one-step sulfurization process at 1,000 °C. SEM and AFM images of sulfurized MoO_x thin film using two-step sulfurization process with first-sulfurization temperatures of (c,d) 600 and (e,f) 800 °C, respectively. Scale bars, (a,c,e) 200 nm and (b,d,f) 0.5 μm.

process at 1,000 °C. In contrast to WS_2 , however, the MoS_2 shows a rough and non-continuous surface, and the measured root mean square (r.m.s.) is much larger (1.4 nm) than that of the SiO_2 substrate (0.37 nm). We surmise that this discrepancy between the MoO_x and WO_3 thin films sulfurized at the same temperature (1,000 °C) is caused by the relatively lower vaporization temperature of MoO_x (~700 °C) in comparison with WO_3 (over 1,100 °C)³¹. In other words, the MoO_x is vaporized before the conversion to MoS_2 is complete, resulting in a rough surface.

Therefore, we examined the effect of sulfurization temperature on the roughness of the sulfurized ALD MoO_x thin film. To achieve this, we conducted a two-step sulfurization process, which consists of a low-temperature first step for the sulfurization of the MoO_x and a high-temperature second step to enhance the MoS_2 crystallinity. The first-sulfurization temperatures were set to lower (600 °C) and higher (800 °C) temperatures than the vaporization temperature of MoO_x (700 °C), while the second-sulfurization temperature and process time were kept at 1,000 °C and 150 min, respectively (see Methods section). The roughness of the sulfurized MoO_x thin films in accordance with first-sulfurization temperature was then compared using SEM and AFM (Fig. 1c–f). Figure 1c,e shows SEM images of the sulfurized MoO_x thin films for first-sulfurization temperatures of 600 °C and 800 °C, respectively. The sulfurized MoO_x thin film at a first-sulfurization temperature of 600 °C has a smooth and continuous surface, while the MoO_x thin film sulfurized at a first-sulfurization temperature of 800 °C has a rough and

non-continuous surface. AFM analyses (Fig. 1d,f) illustrate the variations in the roughness of the sulfurized MoO_x thin films more clearly, which is due to the differing first-sulfurization temperatures. The r.m.s. value for the MoS_2 sulfurized at 600 °C is very low ($\sim 0.4 \text{ nm}$) and is close to the r.m.s. value of the SiO_2 substrate (0.37 nm). In contrast, the r.m.s. value of the MoS_2 in the 800 °C case is relatively high (0.8 nm). As a result, a first-sulfurization temperature of 600 °C results in MoS_2 with uniform and continuous surfaces, due to the fact that the first-sulfurization temperature is lower than the vaporization temperature of MoO_x , as we assumed. Based on this result, we used a two-step sulfurization process with a 600 °C first-sulfurization temperature to synthesize continuous MoS_2 and $\text{Mo}_{1-x}\text{W}_x\text{S}_2$ alloys.

Next, layer-number-controlled MoS_2 was synthesized utilizing the two-step sulfurization process described above. Figure 2a-d shows the AFM images and height profiles of the transferred MoS_2 , which were synthesized by sulfurizing MoO_x thin films deposited by 6, 9 and 12 ALD cycles. The measured thicknesses of the synthesized MoS_2 were ~ 1 , 1.6 and 2.3 nm for 6, 9 and 12 MoO_x ALD cycles, respectively. These thicknesses correspond to mono-, bi- and tri-layer (1, 2 and 3l) MoS_2 , considering that the height of 1l MoS_2 on SiO_2 is $\sim 1 \text{ nm}$ and the spacing between the first and second MoS_2 layers is $\sim 0.6 \text{ nm}$ (refs 3,4). As reported previously, the larger AFM-measured spacing between the first MoS_2 layer and the substrate, compared with that between the MoS_2 layers, is caused by the effect of distinct tip-sample and tip-substrate interactions^{3,30,32}. Also, the apparent colour gains of the transferred 1, 2 and 3l MoS_2 are observed in optical microscopy (OM) images (Supplementary Fig. 2). It should be noted that the MoS_2 is not formed in the case of an ALD MoO_x thin film with an ALD cycle number of < 3 (Supplementary Fig. 3). This is attributed to a nucleation delay during the initial growth of the MoO_x , and similar behaviour was observed during the synthesis of WS_2 by sulfurization of ALD WO_3 (ref. 30). After the nucleation delay, 1l of MoS_2 is formed by the sulfurization of each three-cycle ALD MoO_x thin film sample ($\sim 0.8 - 0.9 \text{ nm}$ in thickness). This observation agrees with a previous report, where

$\sim 1 \text{ nm}$ of MoO_x film transformed into a 1l MoS_2 via sulfurization³³. The stoichiometry calculated from X-ray photoemission spectroscopy (XPS) result is 2 (S/Mo) as shown in Supplementary Fig. 4. As a result, we can systematically control the layer number of MoS_2 by controlling the ALD MoO_x cycle number.

The MoS_2 were further characterized using Raman, PL and high-resolution TEM (HRTEM). The Raman spectra ($\lambda_{\text{exc}} = 532 \text{ nm}$) for 1, 2l and 3l MoS_2 are shown in Fig. 2e. The MoS_2 exhibit in-plane and out-of-plane vibrations modes at 386.6 and 406.5 cm^{-1} (E' and A'_1) for the 1l, 385.6 and 407.6 cm^{-1} (E_g^1 and A_{1g}) for 2l, and 384.7 and 408.5 cm^{-1} (E'^1 and A'_1) for 3l (ref. 34). From the Raman spectra, we calculated the relative peak distance between the in-plane and out-of-plane modes, which is closely related to the layer number of the MoS_2 due to the softening in the in-plane and stiffening in the out-of-plane mode frequencies, with increasing layer numbers^{35,36}. The calculated relative peak distances are 19.9, 22 and 23.8 cm^{-1} for the 1, 2 and 3l samples, respectively, which are in good agreement with previously reported values for synthesized MoS_2 (refs 37–39).

The PL spectra dependence on the layer number of the MoS_2 is shown in Fig. 2f. The spectrum of the 1l MoS_2 shows PL peaks at 1.89 eV and 2.01 eV, which are correlated to the A_1 and B_1 direct excitonic transitions of the MoS_2 , respectively. With increasing layer number, weak PL peaks are observed at 1.87 eV and 2.00 eV for the 2l, and 1.86 eV and 1.99 eV for the 3l. The red shift and low intensity of the PL peaks with increasing layer number is due to the band gap transition from direct to indirect, which is consistent with the dependency of the PL peak on the layer number^{4–6,40}. These Raman and PL results again confirm the layer controllability of MoS_2 using the ALD process. Figure 2g is an HRTEM image for the synthesized 1l MoS_2 . The MoS_2 shows a honeycomb-like structure with lattice spacing of 0.27 nm and 0.16 nm for the (100) and (110) planes, respectively. In addition, sixfold coordination symmetry is observed in the fast Fourier transformation (FFT) image (inset of Fig. 2g). The approximate

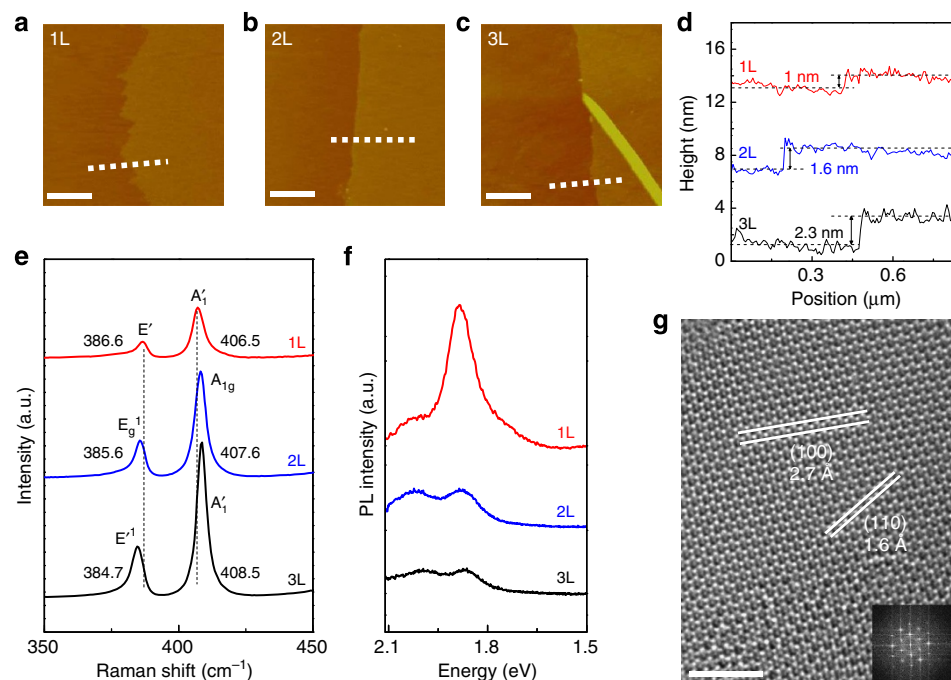


Figure 2 | Characterization of MoS_2 . (a–c) AFM images and (d) height profiles (along with white dashed line in AFM images) of transferred MoS_2 on SiO_2 substrate for 1l, 2l and 3l thickness, respectively. Scale bars, 0.5 μm . (e) Raman spectra and (f) PL spectra for 1l (red), 2l (blue) and 3l (black) MoS_2 on SiO_2 substrate. (g) HRTEM image of 1l MoS_2 at a selected region and (inset) FFT pattern. Scale bars, 2 nm.

domain size is 10–20 nm, similar to that of previously reported synthesized MoS₂ and WS₂ using the sulfurization of MoO_x and WO₃ thin films^{30,41}.

Mo_{1-x}W_xS₂ alloy synthesis. A super-cycle ALD-based Mo_{1-x}W_xS₂ alloy synthesis process was developed based on the synthesis processes for 2D MoS₂ (this study) and WS₂ (previous study)³⁰. The overall synthesis scheme for the Mo_{1-x}W_xS₂ alloy is illustrated in Fig. 3a. First, we conducted 10 cycles of WO₃ ALD to address the nucleation delay of the ALD WO₃ (ref. 30) (not shown in Fig. 3a). Subsequently, one super-cycle ALD process consisting of *n* cycles of ALD MoO_x and *m* cycles of ALD WO₃ was conducted and the deposited Mo_{1-x}W_xO_y alloy thin films were sulfurized. We used varying cycles for MoO_x (*n*) and WO₃ (*m*) in one super-cycle to deposit 0.8–0.9-nm-thick composition-controlled Mo_{1-x}W_xO_y alloy thin films to create a 11 Mo_{1-x}W_xS₂ alloy. This was based on the growth rate of ALD MoO_x (2.7 Å per cycle) and WO₃ (0.9 Å per cycle), as shown in Supplementary Table 1. Figure 3b–d shows the XPS spectra of the 11 MoS₂, 11 WS₂ and sulfurized Mo_{1-x}W_xO_y alloy thin films with different *n* and *m* numbers in one super-cycle. All measured XPS results were normalized by S2p_{3/2} peak intensity and calibrated to the C1s peak at 285 eV. With increasing *n/m* ratio, the intensity of the Mo3d peaks increased, while the W5p_{3/2} and W4f peaks decreased. Furthermore, the peak positions for Mo3d and W4f gradually shifted to higher binding energies, from 232.2 eV and 229.1 eV to 232.5 eV and 229.4 eV for Mo3d_{3/2} and Mo3d_{5/2},

respectively, and from 34.8 eV and 32.6 eV to 35.0 eV and 32.8 eV for W4f_{5/2} and W4f_{7/2}, respectively. In addition, the S2p peaks shifted to lower binding energies, from 163.5 eV and 162.4 eV to 163.3 eV and 162.2 eV for S2p_{1/2} and S2p_{3/2}, respectively. This small shift in peak position is attributed to the enhanced electron attraction strength of S and the reduced electron attraction strength of W, following increased Mo content due to smaller electronegativity of Mo (2.16) than that of W (2.36) as previously reported⁷. It is noteworthy that the Mo⁶⁺ 3d_{3/2} peak, which is attributed to the Mo–O bonding, is not observed in the Mo3d spectra; this indicates the absence of O species.

We calculated the Mo, W and S concentrations from the XPS results for the Mo3d, W4f and S2p peaks, respectively, to examine the Mo_{1-x}W_xS₂ alloy composition. Table 1 presents the calculated concentration and W composition, *x*. The calculated *x* value is dependent on the *n* and *m* numbers in a single super-cycle, and yields *x*=0.8 for *n*=1 and *m*=6, *x*=0.6 for *n*=2 and *m*=4, and *x*=0.3 for *n*=3 and *m*=1. Also, the calculated stoichiometry is 2 (S/(Mo+W)). This shows that the W composition (*x*) in the Mo_{1-x}W_xS₂ alloys can be systematically modulated by changing the values of *n* and *m* in one super-cycle.

The synthesized composition-controlled Mo_{1-x}W_xS₂ alloy from super-cycle ALD Mo_{1-x}W_xO_y alloy thin films were characterized using AFM, Raman and PL, as shown in Fig. 4. The AFM images and height profiles of the transferred Mo_{1-x}W_xS₂ alloys are represented in Fig. 4a–d and they show good uniformity and continuity (also see OM images in

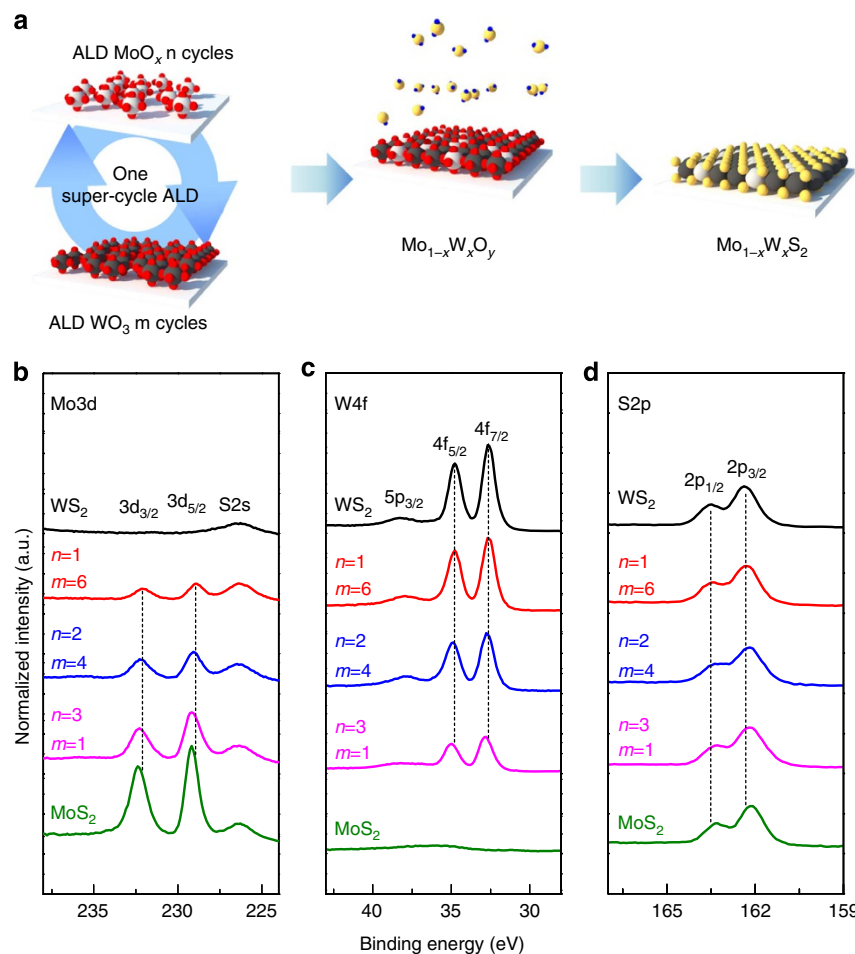


Figure 3 | Synthesis and XPS of Mo_{1-x}W_xS₂ alloy. (a) Synthesis procedure of super-cycle ALD for Mo_{1-x}W_xS₂ alloy. XPS measurements for (b) Mo3d, (c) W4f and (d) S2p core levels in the 11 Mo_{1-x}W_xS₂ alloy with different *n* and *m* numbers in one super-cycle. All measured XPS results are normalized by S2p_{3/2} peak intensity.

Supplementary Fig. 5). The measured thicknesses of the $\text{Mo}_{0.2}\text{W}_{0.8}\text{S}_2$, $\text{Mo}_{0.4}\text{W}_{0.6}\text{S}_2$ and $\text{Mo}_{0.7}\text{W}_{0.3}\text{S}_2$ alloys were all $\sim 1 \text{ nm}$, corresponding to the 1L thickness of $\text{Mo}_{1-x}\text{W}_x\text{S}_2$ alloy. Furthermore, 2 and 3L $\text{Mo}_{1-x}\text{W}_x\text{S}_2$ alloys can be synthesized using two- and three-super-cycle ALD $\text{Mo}_{1-x}\text{W}_x\text{O}_y$ alloy thin films (Supplementary Fig. 6). As a result, our super-cycle ALD-based $\text{Mo}_{1-x}\text{W}_x\text{S}_2$ alloy synthesis process can systematically control the layer number, as well as the composition of the resultant alloys through manipulation of the super-cycle ALD process.

Figure 4e shows the Raman spectra of composition-controlled 1L $\text{Mo}_{1-x}\text{W}_x\text{S}_2$ alloys. The 1L WS_2 ($x=1$) exhibits first-order modes: out-of-plane (A'_1) and in-plane (E') modes at 417 cm^{-1} and 357 cm^{-1} , respectively, and a second-order mode: 2LA(M) at 353 cm^{-1} (ref. 30). The A'_1 mode shifts to a lower frequency with decreasing W composition, while the E' mode related to WS_2 does not noticeably shift with the reduction of intensity. In addition, an E' mode related to MoS_2 appears at $x=0.8$ and shifted to a higher frequency with a reduction in W composition. The specific peak position dependency on W composition is represented in Supplementary Fig. 7, and the W composition

dependence of the Raman spectra of the 1L $\text{Mo}_{1-x}\text{W}_x\text{S}_2$ alloy is consistent with previous reports^{7–9}.

The normalized PL spectra of the composition-controlled 1L $\text{Mo}_{1-x}\text{W}_x\text{S}_2$ alloys are shown in Fig. 4f, also the x values versus the average PL peak positions and s.d. of five-times repeatedly synthesized 1L $\text{Mo}_{1-x}\text{W}_x\text{S}_2$ alloys are plotted in Fig. 4g. As the value of x increased from 0 to 1, the averaged PL peak position initially decreases from 1.885 eV to 1.863 eV , and then gradually increases to 2.021 eV . This non-linear PL peak position behaviour with changing x is the so-called ‘bowing effect’, and has also been reported for other semiconducting alloys and exfoliated 1L $\text{Mo}_{1-x}\text{W}_x\text{S}_2$ alloys^{9,42,43}. The bowing effect in 1L $\text{Mo}_{1-x}\text{W}_x\text{S}_2$ alloy can be described by the Equation (1),

$$\text{EPL,Mo}_{(1-x)}\text{W}_x\text{S}_2 = (1-x)\text{EPL,MoS}_2 + x\text{EPL,WS}_2 - bx(1-x), \quad (1)$$

where b is a bowing parameter. After fitting the experimental results as shown in Fig. 4g (red solid curve), a b value of $0.25 \pm 0.03 \text{ eV}$ was extracted. The extracted b value is comparable to that of the previous experiment ($0.25 \pm 0.04 \text{ eV}$) and simulation ($0.28 \pm 0.04 \text{ eV}$) results⁹. Furthermore, the s.d. of the five-times repeatedly synthesized 1L $\text{Mo}_{1-x}\text{W}_x\text{S}_2$ alloys are small within the range of 0.008 to 0.01, which indicates that the process has good reliability in terms of composition control. Thus, the PL result confirms that we modulate the band gap of the $\text{Mo}_{1-x}\text{W}_x\text{S}_2$ alloy by reliably controlling the composition. Moreover, the band gap can also be modulated by controlling the layer number (see Supplementary Fig. 8).

Figure 5a is the HRTEM image of the 1L $\text{Mo}_{0.4}\text{W}_{0.6}\text{S}_2$ alloy ($x=0.6$). The $\text{Mo}_{0.4}\text{W}_{0.6}\text{S}_2$ alloy shows a periodic atomic arrangement with a honeycomb-like structure and sixfold coordination symmetry, similar to the 1L MoS_2 shown in Fig. 2f. To distinguish between the W and Mo atoms in the 1L $\text{Mo}_{0.4}\text{W}_{0.6}\text{S}_2$ alloy, we analysed the $\text{Mo}_{0.4}\text{W}_{0.6}\text{S}_2$ alloy using STEM

Table 1 | Calculated composition of $\text{Mo}_{1-x}\text{W}_x\text{S}_2$.

One super-cycle	Mo (%)	W (%)	S (%)	W composition x	
n	m				
1	6	6.9	26.5	66.6	0.8
2	4	12.5	19.3	68.2	0.6
3	1	22.5	10.5	67	0.3

Quantification analysis for Mo3d, W4f and S2p peaks depending on n and m number in one super-cycle. The calculation error for the composition is under 1%.

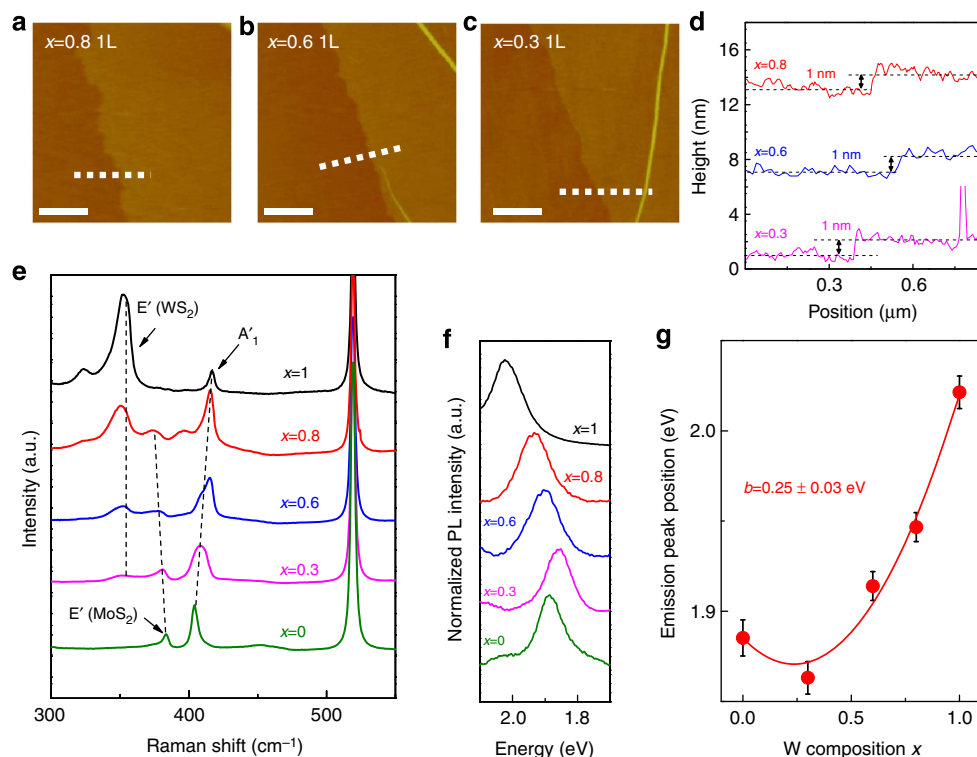


Figure 4 | Characterization of $\text{Mo}_{1-x}\text{W}_x\text{S}_2$ alloy. (a–c) AFM images and (d) height profiles (along with white dashed line in AFM images) of transferred 1L $\text{Mo}_{1-x}\text{W}_x\text{S}_2$ alloy on SiO_2 substrate for $x=0.8, 0.6$ and 0.3 , respectively. Scale bars, $0.5 \mu\text{m}$. (e) Raman spectra and (f) PL spectra for 1L $\text{Mo}_{1-x}\text{W}_x\text{S}_2$ alloy on SiO_2 substrate for $x=1, 0.8, 0.6, 0.3$ and 0 . (g) PL peak position versus W composition (x) graph. Error bars represent s.d. of PL peak position in five-times repeatedly synthesized $\text{Mo}_{1-x}\text{W}_x\text{S}_2$ alloy.

annular dark-field and energy dispersive X-ray spectrometry (EDX). Figure 5b is the STEM-ADF image of the 11 Mo_{0.4}W_{0.6}S₂ alloy. Brighter and less bright spots, which correspond to W and Mo atoms, respectively, are clearly resolved in the ADF image, as previously reported⁴⁴. The calculated Mo/W ratio from the atom count in Fig. 5b is 0.42:0.58, which differs by <5% from the XPS-measured stoichiometry. In addition, the EDX result in Fig. 5c supports the presence of W, Mo and S species in the 11 Mo_{0.4}W_{0.6}S₂ alloy. To extract a clear intensity difference between the W and Mo atoms, we performed an inverse FFT by applying a mask to the yellow dashed square region in Fig. 5b. Figure 5d–e shows the inversed FFT image (Fig. 5d) and intensity profile (Fig. 5e) along with the yellow solid line in Fig. 5d. Although S atoms are not distinguishable in our result as a result of the displacement of S atoms at 200 kV operation voltage by the knock-on mechanism⁴⁵, the W and Mo atoms are clearly observable, confirming that these elements share the metal atom sites⁴⁴. The preference for Mo or W atoms at the neighbouring sites of W atoms is evaluated by degree of alloying that can be calculated by Equation (2)^{23,44},

$$J_W = P_{\text{observed}} / P_{\text{random}} \times 100\%, \quad (2)$$

where P_{observed} is the averaged ratio of number of neighbouring Mo atoms to total neighbouring sites of W atoms, and P_{random} is the total ratio of Mo atoms in the examined layer. Figure 5f represented differently coloured W atoms depending on number of neighbouring Mo atoms: light brown, blue, red, dark red, yellow, green and violet for six, five, four, three, two, one and zero number of neighbouring Mo atoms. The calculated degree of alloying is 99%, which indicate that there is no preference for Mo or W atoms at the neighbouring sites of W atoms and a random mixture of our 11 Mo_{1-x}W_xS₂ alloy.

A VCC Mo_{1-x}W_xS₂ synthesis. The composition controllability of our ALD-based Mo_{1-x}W_xS₂ alloy synthesis process enables synthesis of a VCC Mo_{1-x}W_xS₂ multilayer with a clean interface, strong interlayer coupling and broadband light absorption. We sulfurized a VCC Mo_{1-x}W_xO_y thin film that was deposited by a sequential super-cycle ALD process, so as to synthesize a VCC Mo_{1-x}W_xS₂ multilayer, as shown in Fig. 6a. First, we conducted 20 cycles of WO₃ ALD on a SiO₂ substrate, corresponding to 11 WS₂. We immediately performed three super-cycles of

Mo_{1-x}W_xO_y ALD with different super-cycle n and m numbers, in the following order: $n=1$ and $m=6$, $n=2$ and $m=4$, and $n=3$ and $m=1$. Last, we conducted three cycles of MoO_x ALD ($n=3$) corresponding to 11 MoS₂. The deposited VCC Mo_{1-x}W_xO_y thin film was sulfurized to convert it into a VCC Mo_{1-x}W_xS₂ multilayer. Figure 6b,c shows an AFM image and height profile of the transferred VCC Mo_{1-x}W_xS₂ multilayer, with a measured thickness of ~3.5 nm. This thickness, synthesized by five sequential ALD super-cycles, corresponds to a 51 Mo_{1-x}W_xS₂ alloy, which is consistent with each super-cycle result for the 11 Mo_{1-x}W_xS₂ alloy.

The different composition concentrations of the bottom and top layers in the VCC Mo_{1-x}W_xS₂ multilayer were analysed using angle-resolved XPS (ARXPS). Figure 6d shows the calculated atomic and relative concentration ratios of the Mo and W from the ARXPS measurement (ARXPS spectra are shown in Supplementary Fig. 9). The Mo concentration increased from 18.6 to 20.9%, while the W concentration decreased from 15.7 to 13.5%, with increasing emission angle from 0 to 70° (red line). The Mo/W concentration ratio increased from 1.17 to 1.55 with increasing emission angle (blue line). Although the exact atomic concentration according to position in the VCC Mo_{1-x}W_xS₂ multilayer cannot be calculated because of the larger depth resolution of the XPS measurement in comparison with the VCC Mo_{1-x}W_xS₂ multilayer thickness, the emission angle dependency of the Mo and W concentration indicates Mo-rich and W-rich concentration in the upper and lower layers of the VCC Mo_{1-x}W_xS₂ multilayer, respectively. As a result, ARXPS shows that the VCC Mo_{1-x}W_xS₂ multilayer has VCC characteristics. Notably, the calculated stoichiometry ratio was 2 (S/(Mo + W)) in all ARXPS results.

The formation of Mo_{1-x}W_xS₂ alloy with different compositions in a VCC Mo_{1-x}W_xS₂ multilayer was analysed using Raman spectroscopy. Figure 6e shows the Raman spectrum of a VCC Mo_{1-x}W_xS₂ multilayer, which exhibits strong peaks for A_{1g} MoS₂-like E¹_{2g} and WS₂-like E¹_{2g} + 2LA(M) modes. Each Raman peak can be fitted using a Lorentzian function to the Raman spectrum of the Mo_{1-x}W_xS₂ alloy with $x=0, 0.3, 0.6, 0.8$ and 1. The fitted Raman spectrum was compared with the measured Raman spectrum for the 11 Mo_{1-x}W_xS₂ alloy, with respect to variations in the peak position and peak distances of the A_{1g} and MoS₂-like E¹_{2g} modes, depending on

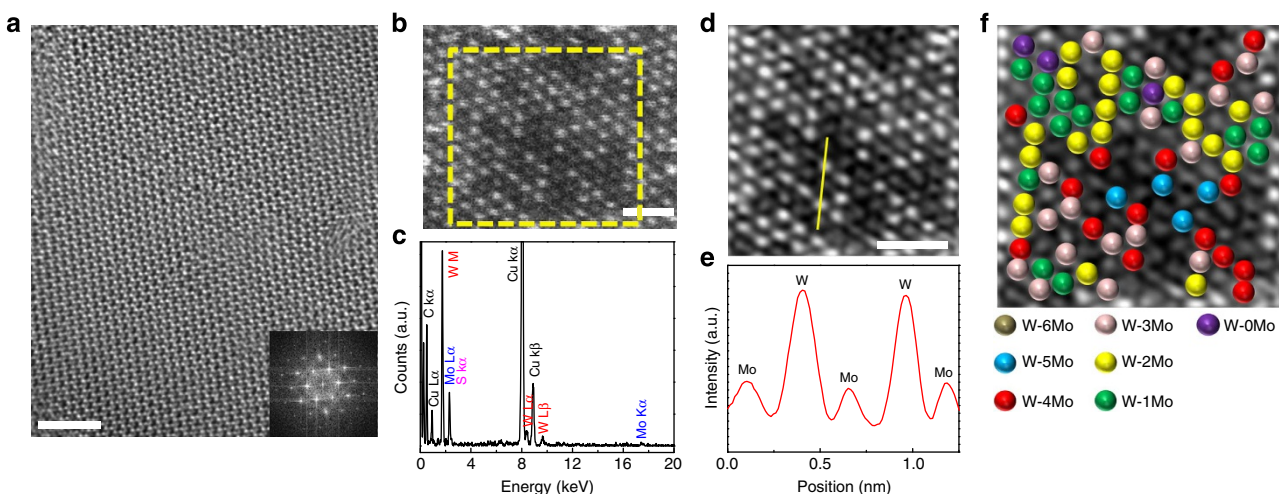


Figure 5 | Atomic arrangement and mixture of Mo_{0.4}W_{0.6}S₂ alloy. (a) HRTEM image of 11 Mo_{0.4}W_{0.6}S₂ alloy at a selected region, and (inset) FFT pattern. Scale bars, 2 nm. (b) STEM-ADF image of 11 Mo_{0.4}W_{0.6}S₂ alloy at a selected region and (c) corresponding EDX spectrum. Scale bars, 1 nm. (d) Inverse FFT image with masking applied to yellow dashed square region in b. Scale bars, 1 nm. (e) Intensity profile of yellow solid line in d. (f) Coloured W atoms with light brown, blue, red, dark red, yellow, green and violet for six, five, four, three, two, one and zero number of neighbouring Mo atoms.

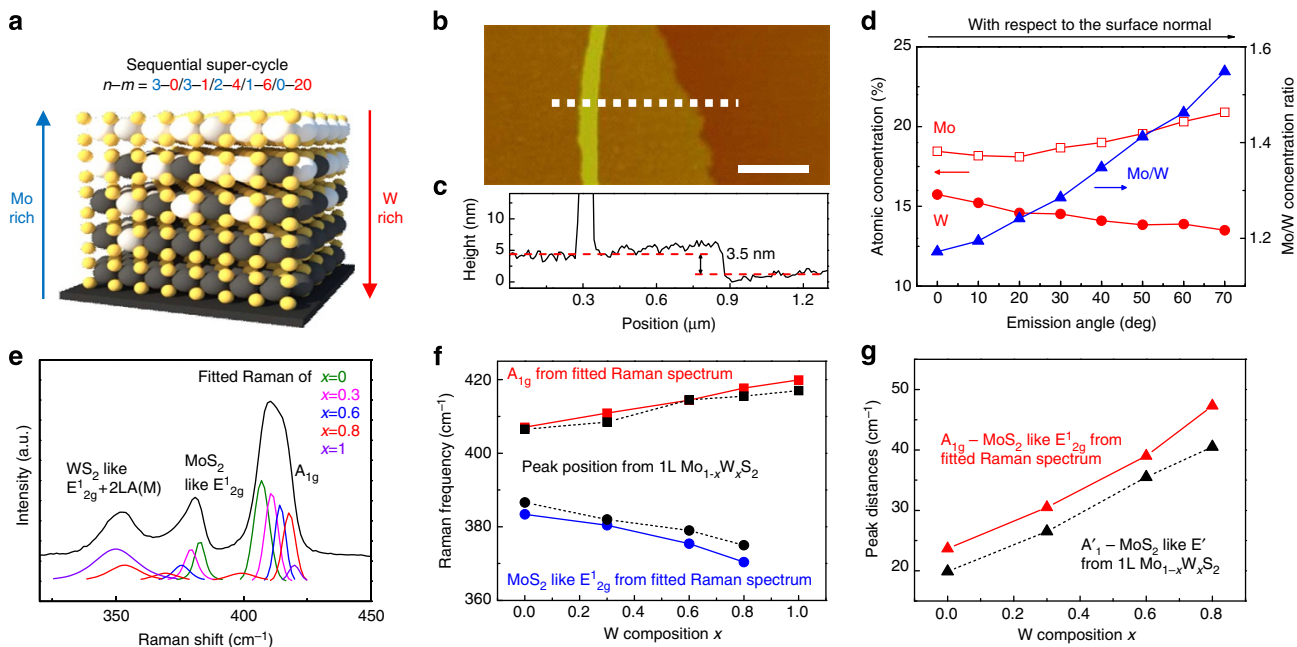


Figure 6 | Characterization of VCC Mo_{1-x}W_xS₂ multilayer. (a) Sequential super-cycle ALD procedure and schematic structure of a VCC Mo_{1-x}W_xS₂ multilayer. (b) AFM image and (c) height profiles (along with white dashed line in AFM image) for a VCC Mo_{1-x}W_xS₂ multilayer. Scale bars, 0.5 μm. (d) Calculated atomic concentration and relative concentration ratio of Mo and W from ARXPS measurement. (e) Raman spectra for a VCC Mo_{1-x}W_xS₂ multilayer. (f) Raman peak position of A_{1g} and MoS₂-like E_{1'2g} modes from fitted Raman spectra (red and blue solid line) and from measured Raman spectra of 1L Mo_{1-x}W_xS₂ alloy (black dashed line). (g) Calculated Raman peak distances between A_{1g} and MoS₂-like E_{1'2g} modes from fitted Raman spectra (red solid line) and from measured Raman spectra of 1L Mo_{1-x}W_xS₂ alloy (black dashed line).

W concentration. The A_{1g} and MoS₂-like E_{1'2g} peak positions from the fitted Raman spectrum are represented in Fig. 6f with the measured Raman peak positions for the 1L Mo_{1-x}W_xS₂ alloy (black dashed line, the same as Supplementary Fig. 7). The variation in the fitted Raman peak position with increasing W concentration in the Mo_{1-x}W_xS₂ alloy is the same as the variation in the measured Raman peak position for the 1L Mo_{1-x}W_xS₂ alloy: A_{1g} shifts to a higher frequency with an increase in W concentration, while the MoS₂-like E_{1'2g} modes downshift. Figure 6g shows peak distances between the A_{1g} and MoS₂-like E_{1'2g} modes from the fitted Raman spectrum (red solid line) and measured Raman spectrum of the 1L Mo_{1-x}W_xS₂ alloy (black dashed line), which are 3–4 cm⁻¹ larger than that of the Raman spectrum of the 1L Mo_{1-x}W_xS₂ alloy. This is due to the softening in the MoS₂-like E_{1'2g} mode frequency and stiffening in the A_{1g} mode frequency. Similar behaviour, that is, increasing peak distances with increasing layer number, is also observed in MoS₂ (refs 35,36) and WS₂ (ref. 30) because of the reduced long-range Coulomb interaction between the effective charges, which is induced by an increase in the dielectric screening. These results for the fitted Raman spectra are in good agreement with the dependency of the peak positions on the W composition given by the measured Raman results, and the dependency of the peak distances on layer number in 2D TMDCs. Thus, we can conclude that the fitted Raman spectra show the formation of a Mo_{1-x}W_xS₂ alloy with different compositions in a VCC Mo_{1-x}W_xS₂ multilayer.

As a result, it can be stated that the ARXPS and Raman results show the VCC characteristics of a VCC Mo_{1-x}W_xS₂ multilayer. Also, these findings indicate that the vertical interdiffusion of the Mo and W atoms during the sulfurization process have no critically effect on the VCC characteristics. A similar result was observed in a previous report, in that MoO_x/WO₃ thin film was converted to MoS₂/WS₂ without the formation of a Mo_{1-x}W_xS₂ alloy, indicating the limited interdiffusion of Mo and W atoms⁴⁶.

Further, it is noteworthy that we verified the validity of ARXPS and Raman measurements as a means of characterizing the VCC Mo_{1-x}W_xS₂ multilayer via characterization of a VCC Mo_{1-x}W_xS₂ multilayer synthesized with a reversed vertical composition profile (see Supplementary Fig. 10).

Since the interlayer coupling affects interlayer transition^{15,21,47,48}, strong interlayer coupling in a synthesized VCC Mo_{1-x}W_xS₂ multilayer was evaluated using comparison of interlayer transition in three difference sample types as shown in Fig. 7a. Sample 1 is a stacked VCC Mo_{1-x}W_xS₂ multilayer fabricated by the transfer of each differently composed Mo_{1-x}W_xS₂ alloy onto glass substrate, while sample 2 is the same as sample 1 but annealed at 200 °C for 15 min in an Ar ambient atmosphere to enhance the interlayer coupling by the removal of residual molecules^{21,48}. Sample 3 is a transferred VCC Mo_{1-x}W_xS₂ multilayer on glass substrate, which was annealed at 200 °C for 15 min in an Ar ambient atmosphere. Ultraviolet-visible spectrophotometer measurements for samples 1, 2 and 3 (Fig. 7b) illustrate that these have broadband light absorption properties due to the sum of the light absorption from the differently composed Mo_{1-x}W_xS₂ alloys. In previous reports, the absorption spectrum of the interlayer transition could be obtained by comparing the intensity difference between the absorption spectra of the weakly interlayer-coupled sample and that of the strongly interlayer-coupled sample^{15,48}. Based on these reports, we extracted the interlayer transition absorption spectrum by subtracting the absorption spectrum of sample 1 from that of sample 2 and of sample 3, since sample 1 has the weakest interlayer coupling of the three samples as a result of the contamination at the interface caused by the layer transfer process^{15,21,48}. The extracted absorption spectra of the interlayer transition are shown in Fig. 7c. The sample 2–sample 1 spectrum (black solid line) shows a small absorbance peak at 1.87 eV, while the sample 3–sample 1 spectrum (red solid line) shows an absorbance peak that is over five times stronger than the sample 2–sample 1 absorbance peak at the same position. Specific observations on the origin of the absorbance peak

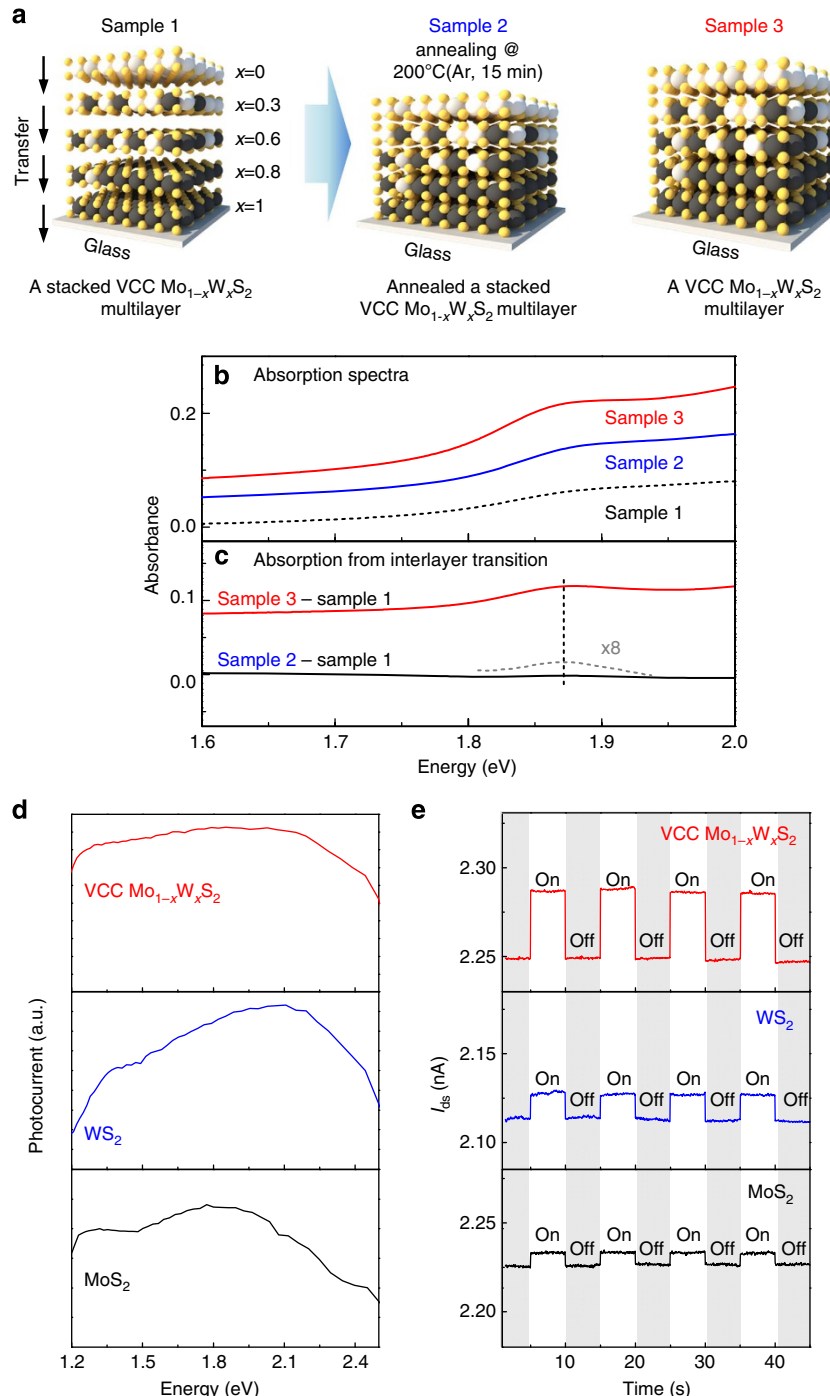


Figure 7 | Absorbance and photoinduced current of VCC $\text{Mo}_{1-x}\text{W}_x\text{S}_2$ multilayer. (a) Schematics of three sample types for ultraviolet-visible spectrophotometer measurement. (b) Absorption spectra of sample 1 (black solid line), sample 2 (blue solid line), and sample 3 (red solid line) and (c) extracted absorption spectra of interlayer transition using subtraction of sample 1 from sample 2 (black solid line) and from sample 3 (red solid line). (d) Spectral and (e) time-resolved photocurrent of a VCC $\text{Mo}_{1-x}\text{W}_x\text{S}_2$ multilayer, 5l WS₂ and 5l MoS₂ photodetectors.

position from the interlayer transition (1.87 eV) are described in the Supplementary Information (Supplementary Fig. 11). The stronger absorbance peak of sample 3–sample 1 in comparison with that of sample 2–sample 1 indicates that sample 3 has stronger interlayer coupling compared with sample 2. In other words, a VCC $\text{Mo}_{1-x}\text{W}_x\text{S}_2$ multilayer based on sequential super-cycle ALD has the strongest interlayer coupling among the three types of samples. We surmise that this strong interlayer coupling results from the absence of a transfer process, which eliminates the incorporation of residual molecules such as H₂O and organic contaminants^{15,21,47,48}.

A VCC $\text{Mo}_{1-x}\text{W}_x\text{S}_2$ multilayer exhibits a broadband light absorption property, as well as strong interlayer coupling. Thus, the VCC $\text{Mo}_{1-x}\text{W}_x\text{S}_2$ multilayer has promising potential use as an active layer in an efficient photodetector. To evaluate the photoinduced response of the VCC $\text{Mo}_{1-x}\text{W}_x\text{S}_2$ multilayer, we observed the spectral and time-resolved photocurrent of a VCC $\text{Mo}_{1-x}\text{W}_x\text{S}_2$ multilayer photodetector and compared it with 5l WS₂ and 5l MoS₂ photodetectors (see the Methods section for details of device fabrication, and see Supplementary Fig. 12 for AFM images of the 5l MoS₂ and WS₂ and their $I-V$

characteristics). Figure 7d shows the dependence of the photocurrent on the illumination energy for the VCC $\text{Mo}_{1-x}\text{W}_x\text{S}_2$ multilayer, 5l WS_2 , and 5l MoS_2 photodetectors for a voltage drain to source (V_{ds}) of 5 V. The continuum power spectral density is represented in Supplementary Fig. 13. The VCC $\text{Mo}_{1-x}\text{W}_x\text{S}_2$ multilayer photodetector generates a broadband photoinduced current from 1.2 to 2.5 eV, because of its broadband light absorption property. In contrast, the 5l WS_2 and 5l MoS_2 photodetectors generate narrower photocurrents than the VCC $\text{Mo}_{1-x}\text{W}_x\text{S}_2$ multilayer, at 1.3 and 2.1 eV for the 5l WS_2 photodetector and 1.2 and 1.8 eV for the MoS_2 device; these values correspond to the 5l WS_2 and MoS_2 bandgaps. We then examined the time-resolved photocurrent measurement using white-light illumination, as shown in Fig. 7e (result using specific laser wavelength is shown in Supplementary Fig. 14). The white light was first turned off for a period of 5 s, and then turned on for 5 s with the biasing $V_{ds} = 5$ V. The drain current (I_{ds}) increased on activation of the light and decayed following removal of the incident light. The induced photocurrents were 39 pA, 13 pA and 11 pA for the VCC $\text{Mo}_{1-x}\text{W}_x\text{S}_2$ multilayer, 5l WS_2 and 5l MoS_2 devices, respectively. Hence, the VCC $\text{Mo}_{1-x}\text{W}_x\text{S}_2$ multilayer generates three to four times greater photocurrent than 5l WS_2 or 5l MoS_2 , which is attributed to broadband light absorption. Thus, we concluded that the VCC $\text{Mo}_{1-x}\text{W}_x\text{S}_2$ multilayer is promising as regards use as an efficient photodetector with broadband light absorption. Furthermore, the broadband light absorption property is feasible for various optoelectronic applications such as solar cells^{49,50}.

Discussion

In summary, we developed an ALD-based $\text{Mo}_{1-x}\text{W}_x\text{S}_2$ synthesis process using sulfurization of super-cycle ALD $\text{Mo}_{1-x}\text{W}_x\text{O}_y$ thin film. We studied the sulfurization process of ALD MoO_x thin films to produce uniform and continuous MoS_2 . The synthesized ALD-based $\text{Mo}_{1-x}\text{W}_x\text{S}_2$ alloy show good stoichiometry, uniform and continuous surfaces, controlled composition and layer numbers, and mixing of Mo and W atoms. Moreover, we developed a simple method to synthesize a VCC $\text{Mo}_{1-x}\text{W}_x\text{S}_2$ multilayer with a clean interface, which shows stronger interlayer coupling than that of a stacked VCC $\text{Mo}_{1-x}\text{W}_x\text{S}_2$ multilayer fabricated using the transfer process. Further, we have shown that the VCC $\text{Mo}_{1-x}\text{W}_x\text{S}_2$ multilayer has promising potential applications as an efficient photodetector, because of its broadband light absorption capability. It should also be noted that the ALD-based TMDCs alloy synthesis process is not only limited to $\text{Mo}_{1-x}\text{W}_x\text{S}_2$, and we expect that similar process strategies can be developed for other TMDCs materials and their vertical stacks.

Methods

Mo_x film growth and characteristics. A 6-inch ALD chamber containing a loadlock chamber was used for the deposition of the MoO_x films. The films were deposited on $\text{SiO}_2(300\text{ nm})/\text{Si}$ substrates by plasma-enhanced ALD using $\text{Mo}(\text{CO})_6$ and O_2 plasma at a 200 °C growth temperature. The temperature of the bubbler containing $\text{Mo}(\text{CO})_6$ was maintained at 35 °C to produce adequate vapour pressure, and vapourised $\text{Mo}(\text{CO})_6$ molecules were transported into the chamber by pure argon (99.999%) carrier gas. The O_2 flow and plasma power were fixed at 300 s.c.c.m. and 200 W, respectively. An ALD cycle consists of four steps: $\text{Mo}(\text{CO})_6$ precursor exposure (t_s), Ar purging (t_p), O_2 plasma reactant exposure (t_r) and another Ar purging (t_p). In the ALD MoO_x process, the t_s , t_p and t_r were fixed at 5 s, 12 s and 5 s, respectively. Optimization of the ALD MoO_x process is described in the Supplementary Fig. 1.

Mo_{1-x}W_xO_y Film Growth. MoO_x and WO_3 ALD processes²⁷ were used to deposit $\text{Mo}_{1-x}\text{W}_x\text{O}_y$ film using super-cycle ALD (as shown in Fig. 3a) under the same chamber and deposition conditions described above for the ALD of MoO_x . After 10 cycles of WO_3 ALD to address nucleation delay²⁷, we conducted super-cycle ALD, which consists of n cycles of MoO_x ALD and m cycles of WO_3 ALD. The detailed process steps are shown in Supplementary Table 1.

Sulfurization processes. *One-step process.* To sulfurize the ALD MoO_x , the sample was placed in the centre of a tube furnace (1.2 inch in diameter). Initially, the sample was heated at 200 °C for 60 min under flowing H_2 (25 s.c.c.m.) and Ar (25 s.c.c.m.) gas, to remove any organic contaminants on the surface. Subsequently, the temperature was gradually increased from 200 to 1,000 °C at 13.3 °C min⁻¹, and this temperature was then maintained for 60 min with flowing Ar (50 s.c.c.m.) and H_2S (5 s.c.c.m.). Then, the sample was cooled to room temperature under a flowing Ar (50 s.c.c.m.) atmosphere.

Two-step process. Initially, samples were annealed at 200 °C as in the one-step process. Then, the temperature was gradually increased from 200 °C to first-sulfurization temperatures of 600 or 800 °C at 13.3 °C min⁻¹. The peak temperature (600 or 800 °C) was maintained for 60 min with flowing Ar (50 s.c.c.m.) and H_2S (5 s.c.c.m.). Subsequently, the temperature was gradually increased from the first-sulfurization temperatures to 1,000 °C at 13.3 °C min⁻¹ and was maintained at this temperature for 30 min with flowing Ar (50 s.c.c.m.) and H_2S (5 s.c.c.m.). The sample was cooled to room temperature under a flowing Ar (50 s.c.c.m.) atmosphere after the process was completed. Based on the results shown in Fig. 1, we used a two-step sulfurization process with a 600 °C first-sulfurization temperature to sulfurize MoO_x and $\text{Mo}_{1-x}\text{W}_x\text{O}_y$ thin films in the MoS_2 and $\text{Mo}_{1-x}\text{W}_x\text{S}_2$ alloy synthesis process.

Transfer of MoS₂ and Mo_{1-x}W_xS₂. The as-synthesized MoS_2 and $\text{Mo}_{1-x}\text{W}_x\text{S}_2$ on the SiO_2 substrate were coated with polymethyl methacrylate (PMMA) by spin coating at 4,000 r.p.m. for 60 s. After curing of the PMMA at 100 °C for 15 min, the samples were immersed in 10% hydrogen fluoride solution to etch the SiO_2 layer. Subsequently, the samples were washed using deionized (DI) water and scooped onto a clean SiO_2/Si substrate. The PMMA was removed by acetone and washed away using isopropyl alcohol.

Characterization of MoS₂ and Mo_{1-x}W_xS₂. OM (Olympus DX51), Raman spectroscopy (HORIBA, Lab Ram ARAMIS; 532-nm laser excitation wavelength), AFM (VEECO, Multimode), PL (SPEX1403, SPEX; 532-nm laser excitation wavelength), absorbance with ultraviolet-visible spectrophotometer (JASCO Corporation, V-650), XPS (Thermo UK, K-alpha), SEM (JEOL Ltd, JSM-6701F), TEM (FEI Titan G2 Cube 60-300; accelerating voltage, 80 kV), STEM and EDX (JEM 2100F; accelerating voltage, 200 kV) analyses were employed to characterize the MoS_2 and $\text{Mo}_{1-x}\text{W}_x\text{S}_2$ alloy, and a VCC $\text{Mo}_{1-x}\text{W}_x\text{S}_2$ multilayer.

Fabrication and characterization of photodetectors. Photodetectors were fabricated from an as-synthesized VCC $\text{Mo}_{1-x}\text{W}_x\text{S}_2$ multilayer, 5l WS_2 and 5l MoS_2 on a $\text{SiO}_2(300\text{ nm})/\text{Si}$ substrate by evaporating Au(40 nm)/Ti(1 nm) electrodes with 100-μm channel length. Electrical measurements were conducted using a Keithley 2400 (Keithley Instruments). The photocurrent was measured by modulating the laser beam with a mechanical chopper (1,000 Hz) and detecting the photocurrent with a current preamplifier and a lock-in amplifier. A monochromator was used for wavelength-dependent measurements of the photocurrent.

Parameters for analysis of XPS and Raman. We used Spectral Data Processor v4.1 for the XPS and Raman spectra fitting. In the fitting analysis of the XPS spectra, the full widths at half maximum (FWHM) were between 1.7 and 1.9 eV, the Lorentzian Gaussian Ratio was 2:8, the energy difference between the Mo3d spin-orbit doublet was set to 3.2 eV and the branching ratio was 2/3. In addition, we used Scofield Relative Sensitivity Factor for calculation of stoichiometry as represented in Supplementary Table 2. For the Raman spectrum fitting analysis, the FWHM was between 7 and 12 cm⁻¹.

References

- Bernardi, M. *et al.* Extraordinary sunlight absorption and 1 nm-thick photovoltaics using two-dimensional monolayer materials. *Nano Lett.* **13**, 3664–3670 (2013).
- Wang, Q. H. *et al.* Electronics and optoelectronics of two-dimensional transition metal dichalcogenides. *Nat. Nanotechnol.* **7**, 699–712 (2012).
- Chhowalla, M. *et al.* The chemistry of two-dimensional layered transition metal dichalcogenide nanosheets. *Nat. Chem.* **5**, 263–275 (2013).
- Eda, G. *et al.* Photoluminescence from chemically exfoliated MoS_2 . *Nano Lett.* **11**, 5111–5116 (2011).
- Mak, K. *et al.* Atomically thin MoS_2 : a new direct-gap semiconductor. *Phys. Rev. Lett.* **105**, 136805 (2010).
- Lee, H. S. *et al.* MoS_2 nanosheet phototransistors with thickness-modulated optical energy gap. *Nano Lett.* **12**, 3695–3700 (2012).
- Liu, H. *et al.* Vapor-phase growth and characterization of $\text{Mo}_{1-x}\text{W}_x\text{S}_2$ ($0 \leq x \leq 1$) atomic layers on 2-inch sapphire substrates. *Nanoscale* **6**, 624–629 (2014).
- Chen, Y. *et al.* Composition-dependent raman modes of $\text{Mo}_{1-x}\text{W}_x\text{S}_2$ monolayer alloys. *Nanoscale* **6**, 2833–2839 (2014).
- Chen, Y. *et al.* Tunable band gap photoluminescence from atomically thin transition-metal dichalcogenide alloys. *ACS Nano* **7**, 4610–4616 (2013).

10. Wei, X.-L. *et al.* Modulating the atomic and electronic structures through alloying and heterostructure of single-layer MoS₂. *J. Mater. Chem. A* **2**, 2101–2109 (2014).
11. Feng, Q. *et al.* Growth of large-area 2D MoS_{2(1-x)Se_{2x}} semiconductor alloys. *Adv. Mater.* **26**, 2648–2653 (2014).
12. Xi, J. *et al.* Tunable electronic properties of two-dimensional transition metal dichalcogenide alloys: a first-principles prediction. *J. Phys. Chem. Lett.* **5**, 285–291 (2013).
13. Lin, Z. *et al.* Facile synthesis of MoS₂ and Mo_xW_{1-x}S₂ triangular monolayers. *APL Mater.* **2**, 092514 (2014).
14. Tannous, J. *et al.* Synthesis and tribological performance of novel Mo_xW_{1-x}S₂ ($0 \leq x \leq 1$) inorganic fullerenes. *Tribol. Lett.* **37**, 83–92 (2010).
15. Yu, Y. *et al.* Equally efficient interlayer exciton relaxation and improved absorption in epitaxial and non-epitaxial MoS₂/WS₂ heterostructures. *Nano Lett.* **15**, 486–491 (2015).
16. Hong, X. *et al.* Ultrafast charge transfer in atomically thin MoS₂/WS₂ heterostructures. *Nat. Nanotechnol.* **9**, 682–686 (2014).
17. Kośmider, K. *et al.* Electronic properties of the MoS₂-WS₂ heterojunction. *Phys. Rev. B* **87**, 075451 (2013).
18. Huo, N. *et al.* Novel and enhanced optoelectronic performances of multilayer MoS₂-WS₂ heterostructure transistors. *Adv. Funct. Mater.* **24**, 7025–7031 (2014).
19. Jung, Y. *et al.* Chemically synthesized heterostructures of two-dimensional molybdenum/tungsten-based dichalcogenides with vertically aligned layers. *ACS Nano* **8**, 9550–9557 (2014).
20. Cheng, R. *et al.* Electroluminescence and photocurrent generation from atomically sharp WSe₂/MoS₂ heterojunction pn diodes. *Nano Lett.* **14**, 5590–5597 (2014).
21. Tongay, S. *et al.* Tuning interlayer coupling in large-area heterostructures with CVD-grown MoS₂ and WS₂ monolayers. *Nano Lett.* **14**, 3185–3190 (2014).
22. Terrones, H., López-Urías, F. & Terrones, M. Novel hetero-layered materials with tunable direct band gaps by sandwiching different metal disulfides and diselenides. *Sci. Rep.* **3**, 1549 (2013).
23. Gong, Y. *et al.* Band gap engineering and layer-by-layer mapping of selenium-doped molybdenum disulfide. *Nano Lett.* **14**, 442–449 (2013).
24. Hyungjun, K. Characteristics and applications of plasma enhanced-atomic layer deposition. *Thin Solid Films* **519**, 6639–6644 (2011).
25. Kim, H. *et al.* Applications of atomic layer deposition to nanofabrication and emerging nanodevices. *Thin Solid Films* **517**, 2563–2580 (2009).
26. Lee, J.-S. *et al.* Atomic layer deposition of Y₂O₃ and yttrium-doped HfO₂ using a newly synthesized Y(PrCp)₂(N-iPr-amd) precursor for a high permittivity gate dielectric. *Appl. Surf. Sci.* **297**, 16–21 (2014).
27. Nam, T. *et al.* Growth characteristics and properties of Ga-doped ZnO(GZO) thin films grown by thermal and plasma-enhanced atomic layer deposition. *Appl. Surf. Sci.* **295**, 260–265 (2014).
28. Kim, W. H. *et al.* Significant enhancement of the dielectric constant through the doping of CeO₂ into HfO₂ by atomic layer deposition. *J. Am. Ceram. Soc.* **97**, 1164–1169 (2014).
29. Brahim, C. *et al.* ZrO₂-In₂O₃ thin layers with gradual ionic to electronic composition synthesized by atomic layer deposition for SOFC applications. *J. Mater. Chem.* **19**, 760–766 (2009).
30. Song, J.-G. *et al.* Layer-controlled, wafer-scale, and conformal synthesis of tungsten disulfide nanosheets using atomic layer deposition. *ACS Nano* **7**, 11333–11340 (2013).
31. Blackburn, P. E. *et al.* The vaporization of molybdenum and tungsten oxides. *J. Phys. Chem.* **62**, 769–773 (1958).
32. Gutiérrez, H. R. *et al.* Extraordinary room-temperature photoluminescence in triangular WS₂ monolayers. *Nano Lett.* **13**, 3447–3454 (2013).
33. Lin, Y.-C. *et al.* Wafer-scale MoS₂ thin layers prepared by MoO₃ sulfurization. *Nanoscale* **4**, 6637–6641 (2012).
34. Terrones, H. *et al.* New first order Raman-active modes in few layered transition metal dichalcogenides. *Sci. Rep.* **4**, 4215 (2014).
35. Li, S.-L. *et al.* Quantitative raman spectrum and reliable thickness identification for atomic layers on insulating substrates. *ACS Nano* **6**, 7381–7388 (2012).
36. Li, H. *et al.* From bulk to monolayer MoS₂: evolution of Raman scattering. *Adv. Funct. Mater.* **22**, 1385–1390 (2012).
37. Ling, X. *et al.* Role of the seeding promoter in MoS₂ growth by chemical vapor deposition. *Nano Lett.* **14**, 464–472 (2014).
38. Schmidt, H. *et al.* Transport properties of monolayer MoS₂ grown by chemical vapor deposition. *Nano Lett.* **14**, 1909–1913 (2014).
39. Yu, Y. *et al.* Controlled scalable synthesis of uniform, high-quality monolayer and few-layer MoS₂ films. *Sci. Rep.* **3**, 1866 (2013).
40. Splendiani, A. *et al.* Emerging photoluminescence in monolayer MoS₂. *Nano Lett.* **10**, 1271–1275 (2010).
41. Lee, Y. *et al.* Synthesis of wafer-scale uniform molybdenum disulfide films with control over the layer number using a gas phase sulfur precursor. *Nanoscale* **6**, 2821–2826 (2014).
42. Van Vechten, J. *et al.* Electronic structures of semiconductor alloys. *Phys. Rev. B* **1**, 3351 (1970).
43. Yin, W.-J. *et al.* Origin of the unusually large band-gap bowing and the breakdown of the band-edge distribution rule in the Sn_xGe_{1-x} alloys. *Phys. Rev. B* **78**, 161203 (2008).
44. Dumcenco, D. O. *et al.* Visualization and quantification of transition metal atomic mixing in Mo_{1-x}W_xS₂ single layers. *Nat. Commun.* **4**, 1351 (2013).
45. Garcia, A. *et al.* Analysis of electron beam damage of exfoliated MoS₂ sheets and quantitative HAADF-STEM imaging. *Ultramicroscopy* **146**, 33–38 (2014).
46. Elías, A. L. *et al.* Controlled synthesis and transfer of large-area WS₂ sheets: from single layer to few layers. *ACS Nano* **7**, 5235–5242 (2013).
47. Gong, Y. *et al.* Vertical and in-plane heterostructures from WS₂/MoS₂ monolayers. *Nat. Mater.* **13**, 1135–1142 (2014).
48. Chiù, M.-H. *et al.* Spectroscopic signatures for interlayer coupling in MoS₂-WSe₂ van der Waals stacking. *ACS Nano* **8**, 9649–9656 (2014).
49. Lin, Q. *et al.* Efficient light absorption with integrated nanopillar/nanowell arrays for three-dimensional thin-film photovoltaic applications. *ACS Nano* **7**, 2725–2732 (2013).
50. Aydin, K. *et al.* Broadband polarization-independent resonant light absorption using ultrathin plasmonic super absorbers. *Nat. Commun.* **2**, 517 (2011).

Acknowledgements

This work was supported by the Center for Integrated Smart Sensors funded by the Ministry of Science, ICT & Future Planning as Global Frontier Project (CISS-2011-0031848), the National Research Foundation of Korea(NRF) grant funded by the Korea government(MSIP) (No. NRF-2014R1A2A1A11052588 and 2011-0013255), and Korea Evaluation Institute of Industrial Technology (KEIT) funded by the Ministry of Trade, Industry and Energy (MOTIE) (Project No. 10050296, Large scale (Over 8) synthesis and evaluation technology of 2D chalcogenides for next generation electronic devices).

Author contributions

J.-G.S. carried out most experiments and analysed the data. G.H.R. and Z.L. contributed to TEM measurement. S.J.L. and J.-M.M. contributed to PL measurement. S.W.S and H.C contributed to photoresponse measurement. C.W.L. contributed to XPS measurement. T.C., H.J. and Y.K. contributed to Raman and AFM measurement. C.D. and C.L.-M. contributed to development and handling of ALD precursor. J.-G.S., J.P. and H.K. designed the experiment and co-wrote the paper. All of the authors discussed the results and commented on the paper.

Additional information

Supplementary Information accompanies this paper at <http://www.nature.com/naturecommunications>

Competing financial interests: The authors declare no competing financial interests.

Reprints and permission information is available online at <http://npg.nature.com/reprintsandpermissions/>

How to cite this article: Song, J. G. *et al.* Controllable synthesis of molybdenum tungsten disulfide alloy for vertically composition-controlled multilayer. *Nat. Commun.* **6**:7817 doi: 10.1038/ncomms8817 (2015).



This work is licensed under a Creative Commons Attribution 4.0 International License. The images or other third party material in this article are included in the article's Creative Commons license, unless indicated otherwise in the credit line; if the material is not included under the Creative Commons license, users will need to obtain permission from the license holder to reproduce the material. To view a copy of this license, visit <http://creativecommons.org/licenses/by/4.0/>